



The Structure Evolution of the Interstitial High Entropy Alloy $\text{Fe}_{50}\text{Mn}_{30-x}\text{Cr}_{10}\text{Ni}_{10}\text{C}_x$ Produced by Mechanical Alloying

Marwa A. Abbas¹ · Doha M. Azzam^{1,2} · Sarah A. Elnekhaily¹ · Samir A. Ibrahim¹

Received: 27 February 2024 / Revised: 14 June 2024 / Accepted: 14 July 2024
© ASM International 2024

Abstract

Three non-equiatomic $\text{Fe}_{50}\text{Mn}_{30-x}\text{Cr}_{10}\text{Ni}_{10}\text{C}_x$ ($x = 0.2, 0.5, \text{ and } 0.8$ atomic%) high entropy alloys were prepared by mechanical alloying with milling times up to 25 h. Green compacting and sintering at 1200 °C for 6 h were conducted to the milled samples. The phase diagram of each of the studied high entropy alloy system was predicted under equilibrium conditions. Microstructure characterization and chemical composition analysis were carried out using x-ray diffraction, scanning electron microscope, and transmission electron microscope. A dual-phase structure is established from the austenitic FCC, with Fe and Ni as the main elements, and the carbide precipitates that have a cuboidal shape and are rich in both Cr and Mn. There is an obvious grain size heterogeneity with some localized grain boundaries decohesion; besides, sigma phase appears at the grain boundaries for all studied alloys. By increasing the C content, both the yield strength and microhardness are enhanced and ductility is decreased with closer values in the higher C content alloys. Compressed alloys show fragmentation and fracturing in cuboidal second phase precipitates, while slip bands are observed in the more ductile FCC grains. In addition, nano-twins are observed in the transmission electron microscope images.

Keywords Carbides · FCC · High entropy alloy · Interstitial carbon · Sintering

Introduction

High entropy alloys (HEAs) have a unique design concept. Up to now, HEAs are usually considered multi-principal element alloys that contain at least four principal elements ranging from 5 to 35 atomic at.% concentrations for each element. HEAs have received significant attention due to their promising mechanical properties, including higher strength and hardness values, increased corrosion resistance, improved thermal stability, and higher electrical conductivity. It was originally designed to produce crystal-line entropy-stabilized massive solid solution phases with equiatomic composition through maximizing configurational entropy. For more information regarding the main concept

of such materials, the reader can refer to [1–4]. Recently, a new design concept was introduced where other factors, rather than the configurational entropy, contribute to the solid solution phase formation [5, 6]. It is also suggested that solid solutions can be stabilized using non-equiatomic quinary and/or quaternary alloy systems [7, 8]. Non-equiatomic compositions potentially have exceptional properties with much more commercial viability. The principle of non-equiatomic HEAs has significantly widened the compositional space for the design of HEAs, and work on these compositions has developed mechanical features that are unsurpassed. In contrast, many studies have shown that controlled microstructure design can successfully modify the mechanical properties of conventional metals and alloys [4, 5].

It is argued that for the formation of solid solutions in HEAs, three thermodynamic parameters are commonly used to characterize the behavior of the constituent elements in multi-component alloys: the atomic size difference, the mixing enthalpy, and the mixing entropy. The atomic size mismatch (δ) is used for estimating the local lattice distortion (LLD) effect in the HEAs matrix and is given by:

✉ Doha M. Azzam
doha.otaz@pme.suezuni.edu.eg; doha.monier@bue.edu.eg

¹ Metallurgical and Materials Engineering Department, Faculty of Petroleum and Mining Engineering, Suez University, Suez 43521, Egypt

² Mechanical Engineering Department, Faculty of Engineering, The British University in Egypt, Cairo 11837, Egypt

$$\delta = \sqrt{\sum c_i(1 - r_i/\bar{r})^2} \cdot 100 \quad (1)$$

where $\bar{r} = \sum_{i=1}^n c_i r_i$, c_i and r_i are the atomic percentage and atomic radius of the element i , respectively. However, the estimation can be somewhat misleading because the same atomic type in different systems can exhibit different atomic radii.

The calculated (δ) can easily related to the measured (LLD) to all the formed solid solutions in HEAs with some deviation being reported [9]. The mixing enthalpy (ΔH) can be defined as the difference between the energy of HEA and the energy of the ground state of the constituent, and its value is usually positive with a few exceptions.

Assuming the case of an ideal solid solution, the mixing entropy (ΔS) can be given as:

$$\Delta S = K_B \sum C_i \ln C_i \quad (2)$$

where k_B is the Boltzmann constant. For equiatomic HEAs, Eq (2) simplified which can be given as:

$$\Delta S = R \ln N \quad (3)$$

where N is the number of alloy compounds, and R is the gas constant at room temperature. ΔH contribute to the free energy (ΔG), $-T\Delta S$, to equal -2.739 kJ/mol for binary equimolar alloy and -3.459 kJ/mol for the quinary equimolar alloy. Therefore, in the alloys with a higher number of principal elements (e.g., $N=5$) the entropy contribution to (ΔG) is comparable to the formation of enthalpy (ΔH) of strong intermetallic compound [10], such as in TiAl alloy. It is important to indicate that despite the importance of those thermodynamic parameters to the formation of solid solutions in HEAs, factors, such as electronegativity, valence electron concentration (VEC), and melting point, also significantly influence the formation of the solid solution phases [11].

In Fe-based HEAs, interstitial elements, especially C and N, can present interesting opportunities regarding the stabilization of the FCC solid solution in addition to its possible contribution to solid solution strengthening [12]. The creation of high entropy alloys through the inclusion of various additives can lead to improved mechanical properties and other unique physical properties that are not present in more traditional alloys [13, 14]. The addition of carbon to high entropy alloys (HEAs) has been shown to result in improved properties including improved strength owing to the grain size reduction and prompting nano-twinning without compromising much ductility [13–15]. Chen et al. [13] indicated that the addition of C improves both strength and ductility of CoCrFeNiMn C_x HEAs when the C content is less than 0.1 at.%. Huang et al. [15] added 0.5 at. % C to FeCrNiCoMn HEA, and as a result, its strength significantly increased.

Arc melt/casting methods have been used to prepare HEA systems. However, due to the drawbacks of diseconomy and restrictions on the size and shape of finished products, those fabrication techniques are not suitable for industrial processing [16]. However, there have only been a limited number of studies on carbon containing HEAs fabricated by the powder metallurgy (PM) route. The advantages of PM over melting metallurgy include low power consumption, less material use, good stability, room temperature processing and near-final forming [17]. Additionally, the HEA synthesized by PM has a finer microstructure and a more homogeneous distribution of the composition. It is crucial to investigate how interstitial carbon affects the microstructure and mechanical characteristics of the HEAs synthesized by PM.

The main objective of the research is to study the effect of adding interstitial C atoms with different at.% on the microstructure and mechanical properties of the produced HEA alloys by mechanical alloying technique. The current investigation suggests a basic non-equiatomic alloy system composed of Fe, Mn, Cr, and Ni elements where substituting the Co element with the less expensive nickel element typically used in similar alloy compositions. Moreover, despite the close resemblance between the two elements' electronic structure, their difference in the initial crystal structure could have an impact on the final alloys' behaviors. The alloys were produced by using mechanical alloying (MA) technique followed by sintering where the process optimum parameters were first determined. MA is a well-known solid-state technique that is described by the milling of elemental powders by repeated welding and fracturing [17]. The strengthening mechanisms could be envisaged for the investigated alloys based on the previous studies on advanced steels. Furthermore, the smaller grain size could influence the alloys' mechanical stability against phase changes.

Experimental Procedures

Materials Preparation

Three non-equiatomic Fe₅₀Mn_{30-x}Cr₁₀Ni₁₀C_x ($x=0.2, 0.5,$ and 0.8 at.%) alloy mixtures, assigned as C0.2, C0.5 and C0.8, respectively, were prepared from elemental powders. The purity for all the principal elements (Fe, Cr, Mn, Ni and C) was above 99.8% with graphite powder as the source of carbon. The particle sizes for the elemental powders ranged from 3 to 45 microns. The milling process was conducted using high-energy ball mill (Fritsch Pulverisette 5) where the process optimum milling time was determined at the first composition. 1 wt.% stearic acid was added as a process control agent to all powder mixtures during milling in hardened stainless steel pots and balls to minimize excessive cold welding during the ball milling process. The balls-to-powder

ratio used was 30:1 with rotational speed of 350 rpm. All powder mixtures preparation and sampling were performed in Mbraun Ar glove box ($O_2 \leq 0.1$ ppm, $H_2O \leq 0.1$ ppm). Different milling times of 1 h, 5 h, 10 h, 15 h, and 25 h were evaluated for the C0.2 alloy. The two other alloys, C0.5 and C0.8, were processed using only 25 h of milling by the high-energy ball mill, as 25 h is considered the optimum parameter. Green compaction of the milled powders was performed using a manual hydraulic powder press (Specac 10 Ton) using a 6 mm diameter die under 2-ton pressure. Sintering was then performed at 1200 °C for 6 h followed by furnace cooling to room temperature. (This heat treatment process will be referred to as homogenization treatment.) To avoid oxidation during the sintering process, samples were first inserted into steel capsules and sealed under an argon atmosphere.

Microstructure Characterization

X-ray diffraction (XRD) was carried out using Cu K α radiation (Malvern PANalytical, Empyrean 3 x-ray Diffractometer Unit) with a scan angle (2θ) of 20–90° for phase characterization of the produced alloys.

Microstructure characterization and chemical composition analysis were carried out using a scanning electron microscope (SEM; Thermo Scientific Quattro S) with energy-dispersive x-ray (EDX) and energy dispersive spectroscopy (EDS Mapping) as well as high-resolution transmission electron microscope (200 kV HRTEM; JOEL JEM 2100, made in Japan). For SEM analysis, specimens were first prepared using a grinding machine with different silicon paper grits of 180, 320, 600, 800, and 1200 followed by polishing using a polishing cloth and 0.3 μ m alumina suspension and finally etched in 5% Nital concentration. Small samples from the compressed alloy for the compositions C0.2 and C0.8 were milled for about 15 minutes in the high-energy ball mill for TEM characterizations.

The differential scanning calorimetry (Labsys DTA-DSC SETARAM apparatus 1000 °C) was used at a constant heating rate of 10 °C/min under the Argon atmosphere to check the thermal stability of the alloy powder. The test was carried out using a C0.2 powder sample of the alloy prepared by mechanical alloying technique for 25 h.

Mechanical Measurements

The microhardness of the produced alloys with a load of 500 gm for a dwell time of 15 seconds on polished samples was conducted using (Qness Micro Hardness Vickers Machine). 10-indentations were recorded for each sample to obtain an accurate average value.

A compression test was carried out using a universal testing machine (IBERTEST, TESTCOM-100 model) with a

strain rate of $1 \times 10^{-3} \text{ s}^{-1}$ at room temperature. Three samples were evaluated for each composition. Test samples were cylinders of 6 mm diameter and 6 mm height.

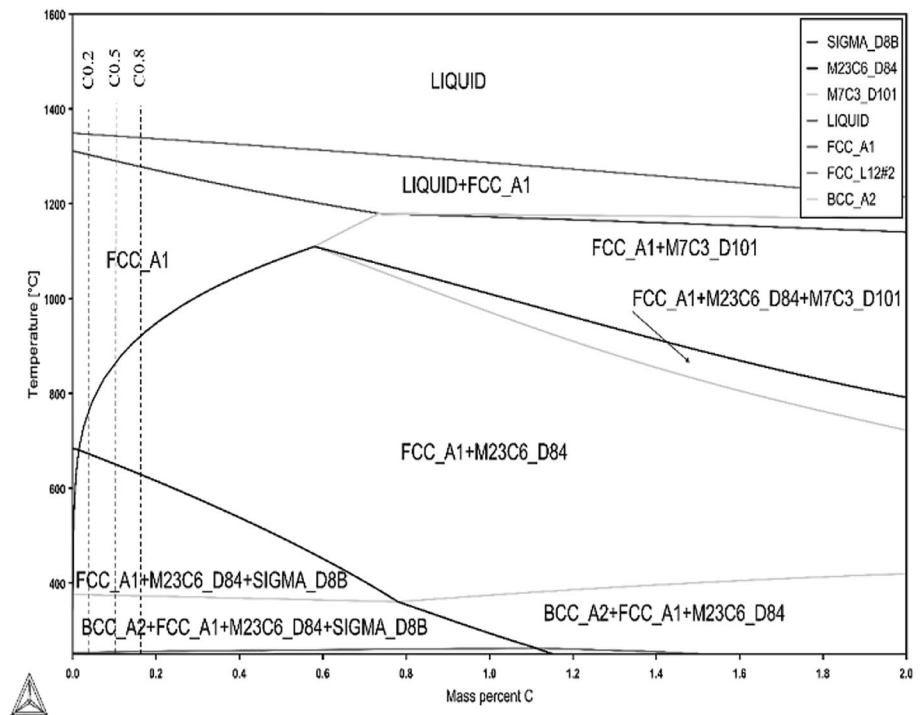
Results and Discussion

Pseudo-Phase Diagram of $Fe_{50}Mn_{30-x}Cr_{10}Ni_{10}C_x$

The phase diagrams of the studied HEAs system were predicted using Thermo-Calc software. The resulting diagram is shown in Fig. 1 as a function of carbon mass percent. This diagram was presented in weight percent as the Thermo-Calc program is dealing only with weight percent. (Guideline illustration for the three alloys was drawn on the figure after converting to equivalent weight percent.) Following the solidification pattern of C0.2, C0.5, and C0.8 alloy compositions, it is possible to observe that the alloys form a single FCC phase which dissociates on cooling into FCC + $M_{23}C_6$ phases *ca.* 790°C, 880°C and 900°C, respectively. The precipitating temperature is higher for alloys with higher carbon contents, indicating an increase in carbon solubility in the FCC solid solution and subsequently an increase in the volume fraction of precipitates. The sigma phase appears to form at lower temperatures ~680°C, ~630°C and ~610°C for C0.2, C0.5 and C0.8 alloy compositions, respectively. It is worth mentioning that Thermo-Calc prediction assumes an equilibrium condition. However, as will be illustrated in the following sections, the microstructure examination confirms that sigma phases existence is related to post-solidification treatment. It is reported in [18] that this phase can appear after an exceptionally long annealing treatment. Thus, during the experimental processing route, the furnace cooling following homogenization treatment could contribute to a sigma phase formation. Similar results were reached for HEAs using the same basic elements [19, 20].

The temperatures and volume fractions of the carbide for the three compositions are shown in Fig. 2a–c. The carbide phase formation temperature is strongly carbon content dependent together with its volume fraction. They both increase with increasing carbon content. SEM images, Fig. 3a–c, show that grain boundaries are smooth with no obvious precipitation suggesting that the basic carbide phase is separately formed in the microstructure. Also, the presence of voids as present in SEM images can be attributed to the sample preparation process for metallographic examinations (grinding, polishing, and etching), which remove the weak particles from the alloy surface. As will be indicated in 3.2.1, the Cr-rich phase is assigned as $M_{23}C_6$ with ($M = Cr, Mn, \text{ and/or } Fe$) and takes a specific morphology (cuboidal shape) but with apparent larger volume fraction compared to the thermodynamic predicted carbide phase which is given to be 0.02 and 0.04% for 0.5 and 0.8% C, respectively. Such

Fig. 1 Thermo-Calc prediction for carbon content in the range 0 to 2 wt.%



differences cannot only be associated with the equilibrium cooling condition. However, it is strongly related to the high density of defects introduced during MA which can enhance both nucleation and volume fraction of a second phase during the homogenization treatment.

The Effect of Carbon

Microstructure Analysis

The mechanically alloyed powders after homogenization treatment produced a two-phase microstructure with similar morphologies observed for the three different carbon contents as shown in Fig. 3. A prevailing phase is detected with a heterogeneous size distribution of average 2.3–2.7 μm with an irregular shape and no changes within milling time, from 15 h to 25 h. Such stable size during milling can suggest a high density of defects accumulated during the milling deformation, and the limited shape change has been restricted because of the pinning effect of the formed second phase. Moreover, nano-grain clusters with a rectangular shape and submicron size between 409 and 420 nm ($<0.5 \mu\text{m}$) are shown to be randomly distributed in the matrix, Fig. 3. During the mechanical alloying process, the high defects concentration is expected to play a significant role in enhancing the diffusion kinetics of different phases formation during homogenization treatment. The mechanical activation energy produced during milling is likely to

accelerate the alloying reaction and result in the observed dual-phase structure.

Crystallite size (D) was also measured using Scherrer Eq [41], as shown in Eq (4):

$$D = \frac{K\lambda}{\beta \cos \theta} \quad (4)$$

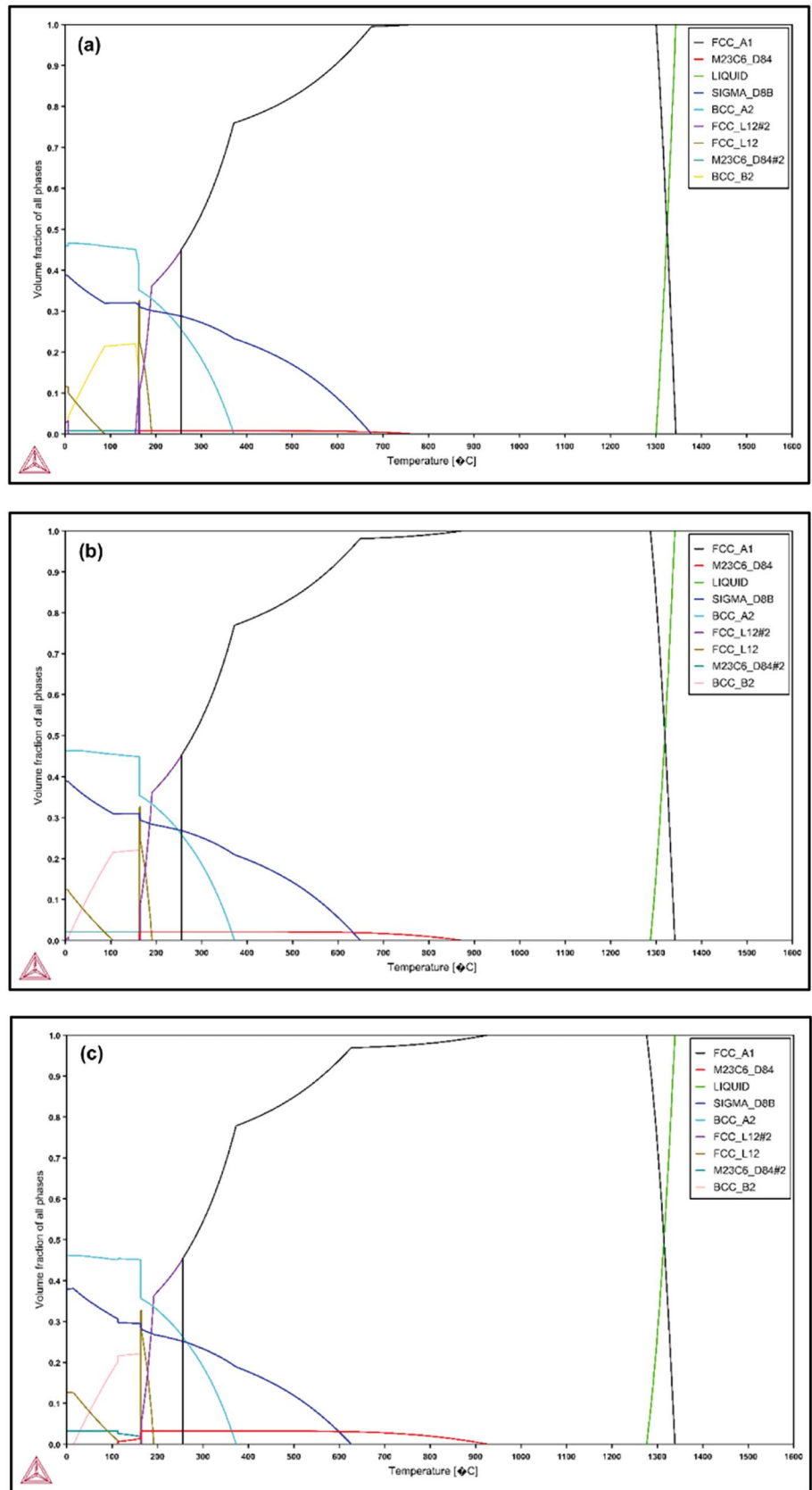
where K is a constant (0.89), λ is the x-ray wavelength (nm), β is the measuring full width at half maximum of peaks, and θ is the peak position. The measured crystallite sizes were 15.9, 19.9, and 15.7 nm for the alloys C0.2, C0.5, and C0.8, respectively. Furthermore, the lattice strain (ϵ) was calculated by using Williamson–Hall's method [42], as shown in Eq (5):

$$\beta \cos \theta = \frac{K\lambda}{D} + 4\epsilon \sin \theta \quad (5)$$

The measured lattice strains were 0.27 %, 0.21 %, and 0.25 % for the alloys C0.2, C0.5, and C0.8, respectively.

The XRD results of the mechanically alloyed systems at different milling times are shown in Fig. 4a, up to 25-h milling followed by sintering. Further, Fig. 4b compares the effect of the final milling time (25 h) after sintering on the different carbon content alloys. The different milling times indicate that the initial mixture elements are associated with Fe, Mn, Ni, and Cr, which are the basic elements of the alloy compositions. The repeated collisions and welding of the particles during milling will cause the diffusion of elements

Fig. 2 Volume fraction calculations for (a) C0.2, (b) C0.5, and (c) C0.8 alloys



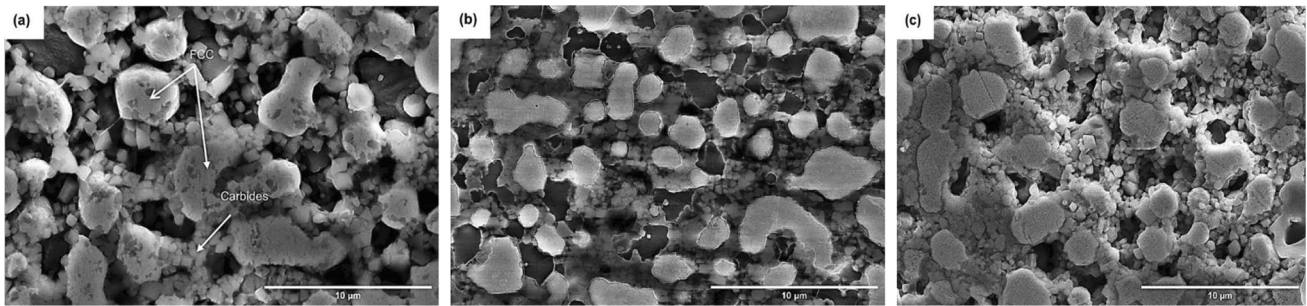


Fig. 3 SEM images of the alloys (a) C0.2, (b) C0.5, and (c) C0.8 milled for 25 h and homogenized

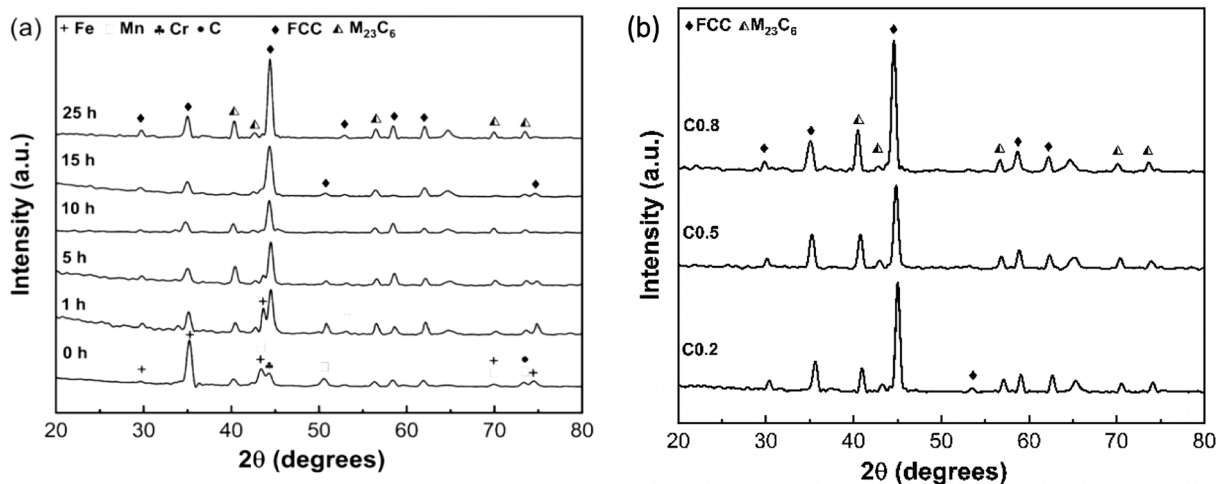


Fig. 4 XRD diffractograms for (a) alloy C0.2 without milling (0 h) and after milling up to 25 h, and (b) alloys C0.2, C0.5, and C0.8 after 25 h of milling and heat treatment (HT)

into each other's lattices. Some observed peaks tend to reduce their intensity or gradually disappear with increasing milling times, which can be associated with new phase formation. No distinct phase differences appear with milling times over 5 hours. There is a slight increase in peak intensities and broadening of the second-phase lines, as shown in Fig. 4a, indicating sluggish diffusion as a process controller. Elements with lower melting points tend to have a higher diffusion rate, and 25-h milling is required for the solid-state reaction between various alloy elements to reach the stable diffraction pattern. The higher stroke milling energy is also likely to contribute to the enhancement of grain refinement observed following the next stage of processing (i.e., homogenization). In addition to that, both phases' microstructures appear to be fully recrystallized after such treatment. A high thermal stability is maintained during this high-temperature process, a behavior that can be associated with the sluggish diffusion frequently observed in HEAs.

XRD patterns of the sintered alloys, Fig. 4, show the presence of two phases structure. The dominating phase is FCC structure with higher peak intensities compared with

second phase lines indexed as $M_{23}C_6$ ($M = Cr, Mn, \text{ and/or } Fe$) as will be discussed later. The different carbon content in these HEA compositions did not have a significant effect on the lattice constant of the FCC phase. The calculated values are ($3.5771, 3.6034, \text{ and } 3.6010 \text{ \AA}$) obtained for the C0.2, C0.5, and C0.8 alloys, respectively, after 25-h milling followed by sintering (homogenization treatment). The grain refined structure is not only enhanced by both the high residual stress and slow elements diffusion but also by the formed second nanophase pinning effect on the grain boundaries movement [21, 22]. This interface pinning can also be related to free C atoms segregation to grain boundaries producing the Zener dragging effects [23]. The latter effect can also be responsible for the dominance of the FCC phase and its thermal stability.

Structure Stability

The thermal stability of the mechanically alloyed powder is evaluated by the differential scanning calorimetry test in the temperature range from room temperature up to

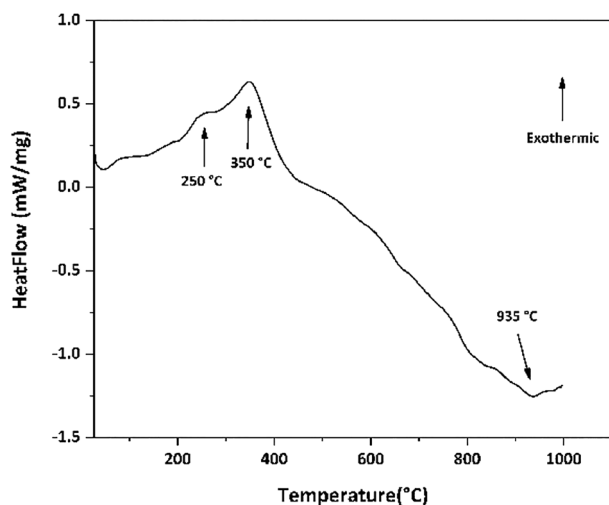


Fig. 5 DSC thermogram of 25-h milling C0.2 alloy heated up to 1000 °C with a heating rate of 10 °C/min

Table 1 EDX results of the matrix and precipitates of alloys C0.2, C0.5 and C0.8 in (wt.%)

| Sample | Phase | Fe | Mn | Cr | Ni |
|--------|-------------------------|------|------|------|------|
| C0.2 | Matrix (FCC) | 75.1 | 2.9 | 3.0 | 19 |
| | Precipitates (Carbides) | 16.7 | 58.6 | 20.4 | 4.3 |
| C0.5 | Matrix (FCC) | 73.7 | 2.1 | 2.8 | 21.4 |
| | Precipitates (Carbides) | 7.4 | 41.7 | 47.7 | 3.2 |
| C0.8 | Matrix (FCC) | 75.3 | 1.9 | 2.6 | 20.2 |
| | Precipitates (Carbides) | 28 | 27 | 38 | 7.0 |

1000 °C. Figure 5 illustrates the DSC trace of the FeMnNiCrC alloy after 25-h milling time for C0.2 alloy. The curve can reveal the non-equilibrium state of the alloy by the broad exothermic reaction in the temperature range from room temperature to 450 °C. This behavior is due to increased lattice strain and the release of internal stress associated with crystal structure changes. Two small exothermic peaks are observed at 250 and 350 °C, and for the current process technique, they are related to stored energy by the milling force. Moreover, the dissociation of the early formed supersaturated solid solution of the mechanical alloying can produce such a small exothermic peak. The current test is extended up to 935 °C without any endothermic peak, indicating that the present alloy composition is thermally stable in this range of temperatures.

Table 1 shows the EDX analysis of alloys C0.2, C0.5 and C0.8 after homogenization. The large particles of the dominating phase in all alloy compositions are enriched in both Fe and Ni and depleted in Mn and Cr elements. This analysis can be associated with the XRD results to confirm the FCC structure dominance known to be a solid solution composed

mainly of iron and nickel [24]. On the other hand, the nano-rectangle phase is enriched in both Cr and Mn elements. These nano-precipitates have a relatively small decrease in size with increasing carbon content. However, they maintain the same cuboidal morphology, suggesting a similar formation mechanism while only differing in the growth rate at higher C compositions. As the carbon composition is less than 1%, it cannot be detected by EDX analysis.

The second phase precipitates size varies from (420 to 409 nm) in their relative alloys with carbon contents of 0.2 to 0.8% C. This agrees well with the thermodynamic prediction, Fig. 2, showing an increasing carbide phase with higher carbon additions. The present results are also in good agreement with several previous studies which also contain Cr-carbide as a second phase as well as the possibility of Cr and Mn-oxide formation [25]. Present EDX results reveal that the high Cr-phase contains an average of 38% Cr, 27% Mn, and 28% Fe wt.% in the C0.8 alloy with a slight difference in the C0.2 and C0.5 alloys. Moreover, there are no Cr-clustering or isolated precipitates with the composition Cr_{23}C_6 observed in the current microstructure, despite that their formation is predicted by thermodynamic calculation. This could be attributed to the fact that Mn-C has the most negative enthalpy (-66 kJ mol^{-1}) followed by Cr-C enthalpy of (-60 kJ mol^{-1}) leading to form a precipitate comprised of Cr, Mn carbide [14]. It has recently been suggested that these carbide precipitates can be observed with either a higher carbon content or by annealing at a relatively low temperature below 800 °C in the equiatomic HEA FeMnCoCrC [24]. The formation of this type of second phase precipitate can be associated with interstitial carbon atoms impact on different phases energies. Yuji & Ikeda [22] in their recent study of interstitial atoms effect on HEAs stability identified that a Cr-rich environment tends to have lower solution energy followed by similar tendency for both Mn and Fe atoms around the interstitial C-atoms. Thus, the creation of Cr-rich-based carbide in these HEAs is promoted by C-atoms preferentially going into the energetically favorable Cr-rich environments. The subsequent carbon depletion in the FCC phase will reduce the SFE and increase the phase stability [26]. This could also suggest that Cr-C bond is energetically more favorable among the other constituent elements. Moreover, it is argued that C-atoms are found to energetically prefer the interstitial sites with lower local valance electron concentration [22]. Then, the creation of Cr-rich carbide with the 3d-transition element HEA is promoted by C-atoms segregation into the energetically favorable Cr-rich area.

Figure 6 shows the element distribution mapping (EDS mapping) of alloys C0.2, C0.5 and C0.8 after homogenization treatment. It confirms the relatively inhomogeneous distribution of Fe, Mn, and Cr- elements that occurred on a localized level among the dual-phase microstructure, as

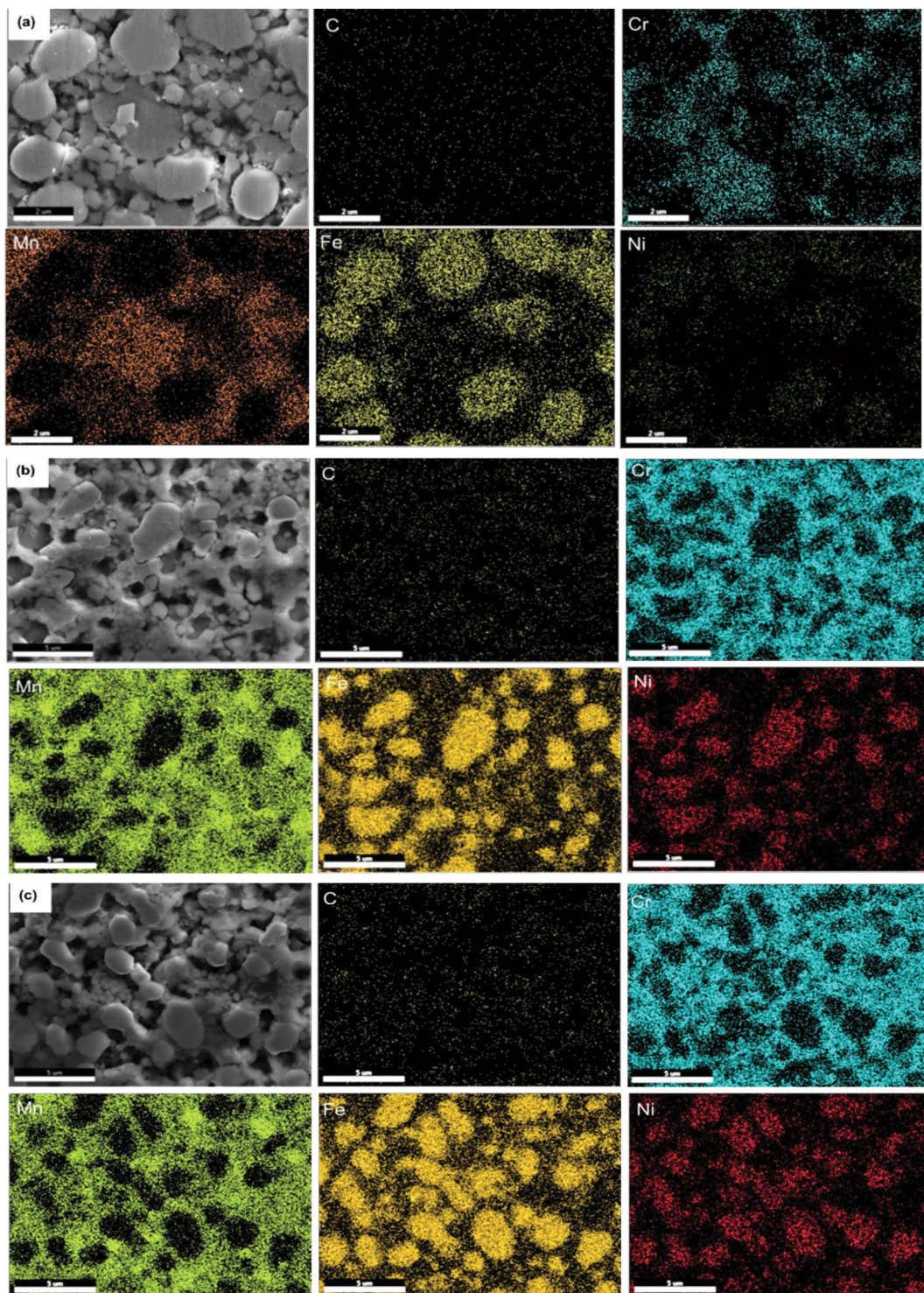


Fig. 6 EDS mapping after 25-h milling and homogenization treatment of (a) C0.2, (b) C0.5, and (c) C0.8 alloys

shown in Fig. 6. Within the limits of experimental measurements, such inhomogeneity is not observed to be carbon dependent. However, on the level of each alloy composition, it is possible to detect composition heterogeneity between grains of the same phase. For example, there is *ca.* 6%

difference in Fe concentration detected for grains with the same FCC structure. An almost similar concentration difference was observed within Cr-enriched nano-grains. It is difficult to attribute this localized chemical heterogeneity to partial recrystallization of the microstructure. However, the

possible formation of complex features during the homogenization of the milled structures, such as micro-twinning, can act as barriers to achieving a homogeneous elemental distribution in addition to the sluggish diffusion nature of HEAs. Further investigation is needed to determine the exact mechanism behind this localized chemical heterogeneity.

Several non-equiatomic HEAs with a single FCC γ -phase show tendency to phase decomposition; possibly a partial transformation to an hcp-phase type structure leading to a dual-phase microstructure [27]. Such change is mainly enhanced with decreasing γ -phase stability at both low and moderate temperatures. This can take place through the destabilizing effect by changing the stacking fault energy of the austenite phase mainly by composition changes or locally by the deformation-induced stacking faults acting as nucleation sites for phase transformation. Therefore, that transformation can occur either thermally and/or by thermo-mechanical process. Recently, in HEAs of the FeMnNiCr system, replacing Ni by Co-addition shows a tendency to induce γ to ϵ phase transformation during thermomechanical treatment [28, 29]. This transformation is highly grain size dependent and is accompanied by local partitioning of alloying elements. Similarly, the highly strained present alloys after MA, also having low SFE, are expected to have such potential for stress-induced transformation of the γ phase [30]. Oppositely, the observed small austenite grain size and the high dislocation density generated during milling can represent, to a large extent, an important barrier preventing the deformation-induced transformation as well as the twinning of the FCC matrix [31, 32]. A high-volume fraction of grain boundaries can hinder the possible growth of the hcp phase and thus suppress phase transformation [33, 34].

The Microstructure Heterogeneity

The present HEAs possess a high degree of grain size heterogeneity that ranges from nano- to micro-scale grain size. This could be mainly due to the processing conditions which enhanced the formation of a dual phases' microstructure. Based on their chemical composition, their solubility limits will differ with a subsequent effect on both phases' stability and properties, for example, the tendency for twinning formation. Such tendency can generally be associated with composition inhomogeneity due to the Mn-atoms depletion from certain grains, resulting in lowering the SFE in these zones [13]. Lowering Mn content due to the Cr-Mn phase formation, as indicated by EDX analysis, Table 1, will lead to a decrease in the γ -phase stability and to an increase of the possibility of SF and twins' formation even though, at present processing condition, such annealing twinning formation is not observed within the SEM limit [26].

Another factor that contributes to heterogeneity is the carbon distribution. Carbon is known to have a retarding effect on recrystallization, and mapping analysis shows a higher carbon content in the second Cr-enriched phase. It is therefore expected that due to differences in both phases chemical analysis and their melting temperatures, recrystallization will occur at different rates. However, it appears that such difference has no effect on the completion of recrystallization since there were no un-recrystallized zones observed for both phases following homogenization treatment. The fully recrystallized structure is attributed to the high stored strain energy during milling in addition to the long annealing time (6 h). A higher rate of nucleation can be associated with the observed nanograins phase and a lower rate for the primary γ -phase, leading to such gradient grain formation across the two-phase microstructure.

The above-discussed heterogeneity strongly suggests that the strengthening inhomogeneity could prevail due to the incompatibility of elastic and plastic deformation between hard and soft phases [35]. This could be due to the local strain difference between softer FCC phase and the second hard parts. Such effect is not only manifested during plastic deformation, but it can be extended to phase stabilities.

In the current work, the microstructure of the studied alloys, after homogenization, exhibited some localized grain boundaries decohesion as shown in Fig. 7, which can be associated with grain boundaries (GBs) embrittlement. This phenomenon could be related to the multiple principal elements' segregation and to a less degree of the strain partitioning across boundaries between incompatible grains. Otto et al [18] in their work on HEAs suggested that elements segregation to grain boundaries can be responsible for significant reduction in ductility due to the produced interface weakening. The residual strain generated by the heavy cold deformation during processing can also promote the diffusion of Cr into the GBs and during subsequent homogenization, enhancing Cr-rich σ - brittle phase formation. A similar

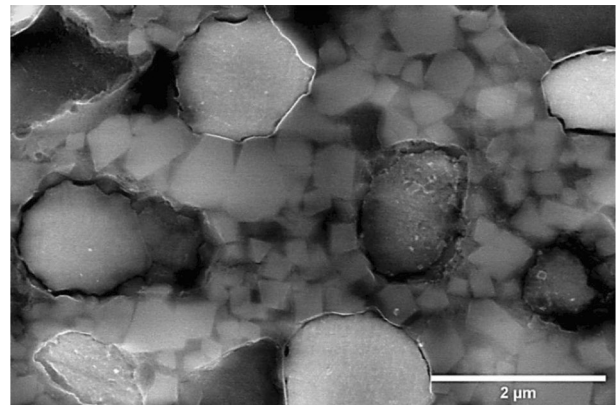


Fig. 7 Grain boundaries decohesion after homogenization

phenomenon has been reported to take place in the HEAs, CrMnFeCoNi system [36]. Also, in the high Mn steel, it was shown that Mn segregation to GBs can induce embrittlement by reducing the GBs cohesion [37, 38]. For the present alloy system, it is known that Mn has a lower diffusivity in austenite compared to Ni and the nano-Cr-rich particle can create a flux of Mn into the austenite grains. Compatibly with this argument, the alloys EDX analysis shows that the FCC phase is depleted in Mn while the Cr-rich phase has a high Mn content in alloys with more than 0.2% C, Table 1. Then, a strong partition and segregation can be expected to occur at the interface of the Cr-enriched phase and grain boundaries [39]. This could explain the relatively low ductility observed during the compression loading of the currently examined alloys, as will be shown later.

It is therefore possible to suggest that in general the grain-refined dual-phases HEAs with compositional heterogeneity are expected to show low plastic formability and brittle fracture at localized levels and consequentially reduced the total alloy ductility.

Sigma-Phase Precipitation

The application of the Thermo-Calc on the current investigated HEAs had predicted the possible sigma phase formation in the non-equiatomically used compositions with different carbon content. Only a limited number of XRD peaks in different composition alloys can be indexed as a tetragonal structure sigma phase, Fig. 4. Only a limited number of XRD peaks in different composition alloys can be observed in the range $41^\circ < 2\theta < 49^\circ$ with small intensities and mostly matched with the carbide peaks. Similar peaks detection assigned those diffraction lines to σ phase with a tetragonal structure [40]. Further confirmation is needed. Moreover, the sigma phase can be detected in some SEM images as shown, for example, in Fig. 8a and b for C0.5 alloy where

a thin white film is observed at the grain boundaries of the FCC phase and extended along many boundaries.

A similar observation in non-equiatomically $\text{Fe}_{20}\text{Co}_{20}\text{Mn}_{20}\text{Cr}_{26}\text{Ni}_{14}$ alloy with nano-size and thermal treatment suggested that sigma phase formation can be enhanced by an extended annealing time below 1070 °C [43]. It also can be associated with both reducing Ni-content and increasing Fe in such HEAs [43, 44]. Both phases, sigma and the FCC, can co-exist when the valence electron concentration (VEC) value is lower than 7.84 [45]. The present alloys have a lower Ni-content regarding the equiatomically composition as well as a low VEC which equals ~ 7.68 , calculated for 0.5 % C alloy, all of which are expected to enhance the sigma phase formation. Moreover, MA can also accelerate sigma phase formation by increasing the defects density promoting high Cr-diffusion pathways and lowering the nucleation barrier [46].

Mechanical Properties of Interstitial HEAs

The present interstitial HEAs with C-atoms content are tested by compression loading as shown in Fig. 9. Table 2 presents the mechanical properties measured under compression and the standard deviation for C0.2, C0.5 and C0.8 alloys after homogenization. A slight increase in both yield strength and maximum compressive strength is observed with increasing the carbon concentration, *e.g.*, the former increased by *ca.* 20% at the highest C content 0.8 at.% compared with 0.2 at.% C. This relative increase can be associated with solid solution strengthening by C addition. On the other hand, a slight reduction in the homogeneous elongation by *ca.* 14% was found for the same change in carbon content. Such small changes can be due to the large microstructure similarity between the alloys despite their different carbon content, as shown previously.

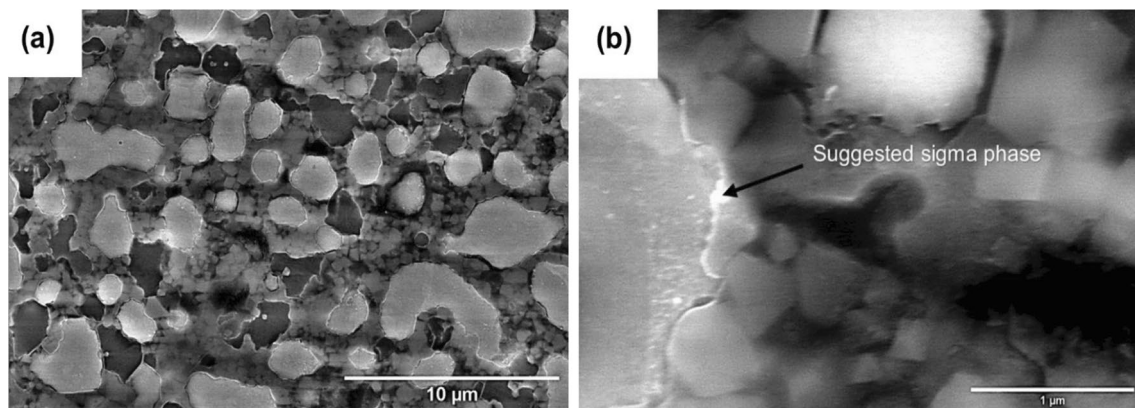


Fig. 8 SEM images for 0.5 % C alloys (a) a thin white film (sigma phase) at the grain boundaries of the FCC phase, and (b) enlarged grain boundary zone

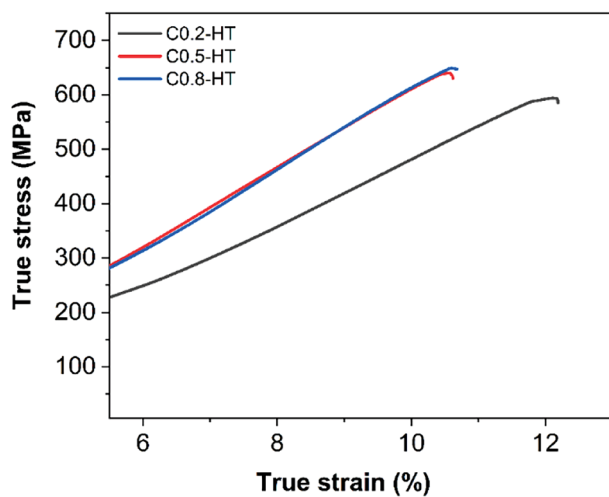


Fig. 9 Stress–Strain curve for different carbon content alloys, C0.2, C0.5, and C0.8

Table 2 Mechanical properties for the alloys C0.2, C0.5 and C0.8 measured by compression test

| Carbon content | C0.2 | C0.5 | C0.8 |
|-----------------------------------|-------|-------|------|
| Yield strength, MPa | 230 | 270 | 275 |
| Maximum compressive strength, MPa | 594 | 640 | 649 |
| Standard deviation | 35.35 | 41.92 | 64 |
| Elongation, % | 12.2 | 10.6 | 10.7 |
| Microhardness, $h_v \pm 10$ | 297 | 322 | 345 |
| Standard deviation | 4.36 | 27.3 | 8.47 |

An attempt to explore the responsible strengthening mechanism is conducted by plotting the work hardening rate $\frac{\partial \sigma}{\partial \epsilon}$, against true stress as well as true strain as shown in Fig. 9a and b. The initial high work rate fast drops with either true stress or true strain indicating a high rate of recovery for the dislocations generated at the early deformation stage. The lowest drop occurred in the C0.2 alloy. As the true strain increases, the hardening rate gradually rises, and the maximum attained strain hardening values for all alloys show a strain-dependent behavior. Such value reached 6600 MPa and 5000 MPa for C0.2 and C0.8 alloys, respectively. Although there is a similar hardening rate behavior for the three alloys compositions, the distinguished stages for each curve take place at different strain and work hardening rates. Such behavior can be attributed to differences in composition and its consequent effect on the relative deformation mechanism.

A similar strengthening trend is observed when comparing the Vickers microhardness measured values. The HV value increases with higher carbon content alloys, Table 2, matching with the compression test results. It is important

to note that the Vickers micro-indentation is still large compared to various microstructural features in the specimens. Thus, the different hardness reading is representative of alloy divergent phases deformation behavior.

The dominated dual-phase microstructure can create strain partitioning between the soft FCC phase and the hard second phase precipitate which leads to a high strain accumulation at the interphase boundaries [47]. This strain can hinder further dislocation gliding, enhancing the strain hardening capacity and consequently higher stresses will be needed to activate the dislocation plasticity. Moreover, a dislocation interaction with the formed stacking faults will further strengthen the matrix and at the higher achievable strain could be accommodated by nano-twins formation. A similar suggestion is adopted in [48] to explain the high plasticity in HEAs composed of the basic FeMnCoNiC elements.

At a high deformation strain, nano-twins formation is likely to take place in a material with a low stacking fault energy (SFE), between (18–35 mJ/m²), and to show a dependence on the chemical composition as well as microstructure features such as grain size [12]. Carbon addition to HEAs is known to increase the SFE [22]. This implies that placing C-atoms at the stacking fault (SF) will be thermodynamically unfavorable, i.e., carbon is likely to segregate to the bulk of the materials. This is consistent with other experimental findings that SFE increases due to carbon addition to HEAs with 3d-transition elements [26, 49] and been associated with a higher tendency for twinning induced deformation.

Twinning formation in general requires a high applied strain with a material with relatively low yield strength at room temperature since high stress is required for its nucleation [50]. SFs and deformation twins are expected to form when their critical stress is overcome by resolved shear stress which is correlated with the applied normal stress through M , the Taylor factor. The critical stress for deformation twinning can be calculated by taking its grain size dependence into consideration as proposed by Sun et al. [50]:

$$\sigma(t) = M \frac{\gamma}{b} + \frac{K}{\sqrt{d}} \quad (6)$$

b is partial dislocation Burgers vector ($1.46 \cdot 10^{-8}$ m) in FCC materials, K is Hall–Petch constant for twinning (980 MPa \sqrt{m}), d is the average grain size, and M is the Taylor constant, depending on carbon content, given the values (3.067, 3.237, and 3.226) for C0.2, C0.5, and C0.8 alloys, respectively. An estimation of the SFE (γ) for HEAs with similar composition to the presently used alloys is found to be between (18–22 mJ m⁻²) with an increase of (7 mJ m⁻²) for each 1% C addition [22]. Substituting “Eq (6)” with the lower and upper limits of such SFE values gives an estimated $\sigma(t)$ of 401.5 MPa and 527.4 MPa, respectively.

The work hardening rate curves, in Fig. 10, indicate that the necessary critical stress for twinning nucleation is reached during the compression testing. Therefore, it is possible to associate the rise in work hardening rate with increasing the stress during deformation to expect nano-twinning formation. However, it is not detected by the SEM inspection. These results also indicate that the deformation twinning formation is carbon dependent. Still, it is difficult to attribute any effective role for grain size since they do not vary much with carbon during processing. The measured average size of the second phase in C0.8 alloy is about (0.4 μm) which is relatively large, and its strengthening is expected to be through the Orowan-type mechanism [51].

Deformed Microstructure

Compressed microstructure of the produced alloys is examined using SEM. Results show a general deformation of the co-existing main FCC and cuboidal second phase precipitates. Figure 11 shows the established microstructure for the 0.2 % C alloy, where the relatively softer FCC phase did not change its shape following the application of compression strain up to fracture, suggesting a restricted deformability most likely by the surrounding second phase precipitates. However, the observed slip bands inside the austenitic grains are an indication of an effective plastic deformation in a ductile behavior mode [40]. Figure 11 also shows a fragmented cuboidal phase and a particle appeared with a crossing crack indicating the brittle nature of the phase precipitates and explained the limited ductility of the alloys in general.

A careful powder specimen was prepared from the compressed alloys for both C0.2 and C0.8 for TEM examination to understand the evolution of the microstructures during the deformation process. The bright field image in Fig. 12a and b shows the continuous presence of a refined

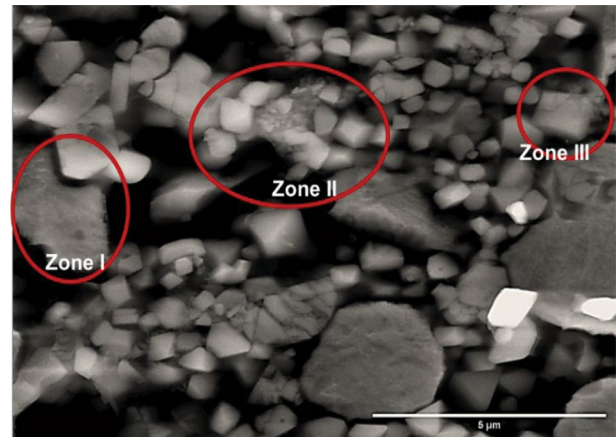


Fig. 11 SEM of C0.2 alloy after compression revealing three different zones. Zone I shows the slip band formation, zone II captures a fragmented cuboidal second phase, and in zone III a cuboidal-shaped particle with a crack crossing it from edge to edge

grain polycrystalline structure in 0.2% and 0.8% C alloys. In some grains, a series of parallel nano-laminates appears, likely nano-twins with an average length of (20–25 nm), and their orientation is dependent on the grain orientation. This suggests a fixed nano-lamination-matrix interface relation. Comparable results indicate that similar microstructures take place in low SFE high entropy alloys [52] which had associated such lamination formation from FCC to HCP phase transformation and/or nano-twins formation. It has been indicated that phase transformation is quite possible during thermomechanical processing of the HEAs with reversible behavior of the reaction [53]. Such transformation is stress enhanced and can be related to low SF zones formed during compression as shown in Fig. 12.

Figure 13 shows the fast Fourier transformation (FFT) of the HRTEM image and gives an estimated d-value of

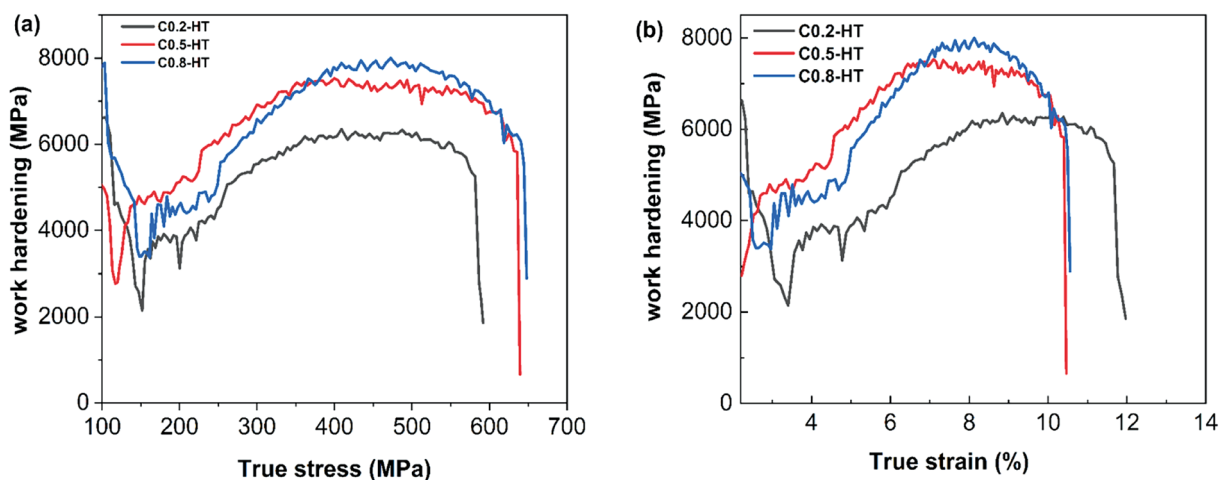


Fig. 10 Work hardening curves for different carbon content alloys (a) vs. stress, and (b) vs. strain

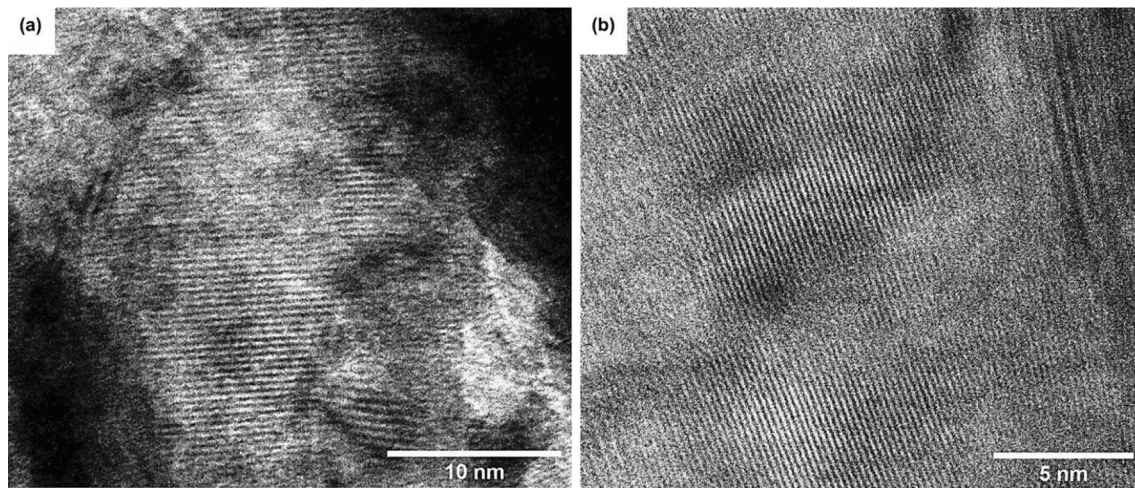


Fig. 12 Bright field image HRTEM for the alloys (a) C0.2, and (b) C0.8

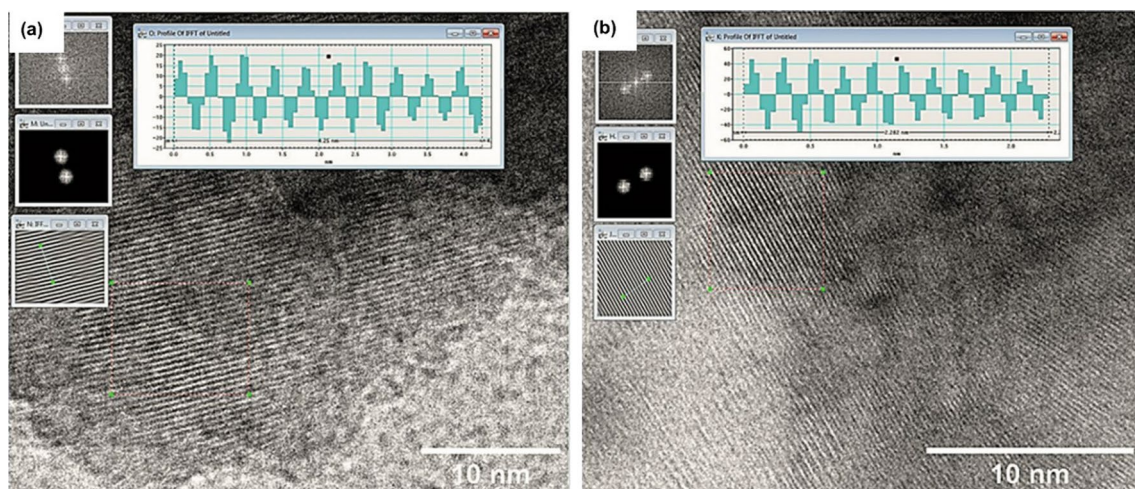


Fig. 13 The fast Fourier transformation of HRTEM for both (a) C0.2 alloy and (b) C0.8 alloy

(0.22 nm) which can be associated with the (111) plane. This value is slightly higher than that obtained by XRD measurement of the homogenous alloy. Such difference can be due to an accepted degree of experimental error as well as the strain effect on the lattice after compression in HRTEM samples. Furthermore, the lattice fringes appear distorted indicating diverse types of atoms in the solid solution. Such lattice distortion is one of the proposed core effects of HEAs [54].

Figure 14 is a selected area diffraction pattern (SAED) of the deformed C0.8 alloy showing a typical polycrystalline powder structure. The diffuse scattering streaks appearing on the diffracted spots can be an indication of stacking faults formation in the polycrystalline structure. High accumulation of dislocations may also affect the diffracted spots producing irregular spots indicating high-strain crystalline structure. Moreover, the presence of spots around the main

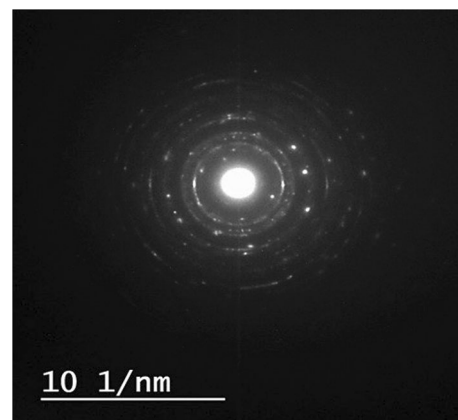


Fig. 14 SAED for the deformed C0.8 alloy sample

ones in the diffraction plane is associated with twinning formation as the twinning orientation is different from the crystal lattice. The direction of the reflected planes inside the twinning is different from the crystal structure and extra spots become visible in the diffraction pattern.

Conclusions

- MA technique followed by high temperature sintering was used to synthesize the non-equiatomic $\text{Fe}_{50}\text{Mn}_{30-x}\text{Cr}_{10}\text{Ni}_{10}\text{C}_x$ ($x=0.2, 0.5$ and 0.8 at.%) HEAs.
- The detected microstructure was mainly FCC with second phase precipitates of M_{23}C_6 type where M can be Cr, Mn and/or Fe and a thin film of sigma phase observed on grain boundaries.
- The acquired structural experimental results are in good match with the Thermo-Calc phase diagram prediction except for the latter higher volume fraction estimation for the sigma phase.
- Grain refinement, with an average grain size ($2\text{--}3\ \mu\text{m}$) of the matrix and a nanosized cuboidal second phase ~ 400 nm, was a direct outcome of the adopted processing technique.
- The synthesized HEAs showed a maximum compressive strength of 649 MPa with 10 to 12% elongation. The studied alloys revealed solid solution, grain boundaries, dislocation interaction and submicron second phase hardening effects.
- The difference in C content within the studied system from 0.2 to 0.8 at.% did not show a highly significant difference in the mechanical behavior. This was associated with obvious microstructure heterogeneity facilitating crack formation and propagation at grain boundaries.
- Evaluation of the alloys work hardening rate profile with both stress and strain indicated possible nano-twins formation in addition to the forementioned strengthening mechanisms.
- The HRTEM images and SAED of the deformed high C alloy ($\text{Fe}_{50}\text{Mn}_{29.2}\text{Ni}_{10}\text{Cr}_{10}\text{C}_{0.8}$) confirmed the nano-twins formation with an average length of 20–25 nm.

Acknowledgements The authors are grateful to the Science and Technology Development Fund (STDF) funding project No. 22854, which made facilities available at the Sustainable Energy Lab, Suez University.

Declarations

Conflict of interest The authors declare that they have no known competing financial interests or personal relationships that could have appeared to influence the work reported in this paper. There are no conflicts to declare.

References

1. D.B. Miracle, O.N. Senkov, A critical review of high entropy alloys and related concepts. *Acta Mater.* **122**, 448–511 (2017). <https://doi.org/10.1016/j.actamat.2016.08.081>
2. M. Vaidya, G.M. Muralikrishna, B.S. Murty, High-entropy alloys by mechanical alloying: a review. *J. Mater. Res.* **34**, 664–686 (2019)
3. J. Chen, X. Zhou, W. Wang, B. Liu, Y. Lv, W. Yang, D. Xu, Y. Liu, A review on fundamental of high entropy alloys with promising high-temperature properties. *J. Alloys Compd.* **760**, 15–30 (2018)
4. E.P. George, D. Raabe, R.O. Ritchie, High-entropy alloys. *Nat. Rev. Mater.* **4**, 515–534 (2019)
5. Z. Li, D. Raabe, Strong and ductile non-equiatomic high-entropy alloys: design, processing, microstructure, and mechanical properties. *JOM.* **69**, 2099–2106 (2017)
6. C.C. Tasan, Y. Deng, K.G. Pradeep, M.J. Yao, H. Springer, D. Raabe, Composition dependence of phase stability, deformation mechanisms, and mechanical properties of the CoCrFeMnNi high-entropy alloy system. *JOM.* **66**, 1993–2001 (2014). <https://doi.org/10.1007/s11837-014-1133-6>
7. F. Zhang, C. Zhang, S.L. Chen, J. Zhu, W.S. Cao, U.R. Kattner, An understanding of high entropy alloys from phase diagram calculations. *Calphad.* **45**, 1–10 (2014). <https://doi.org/10.1016/j.calphad.2013.10.006>
8. A. Kumar, A. Singh, A. Suhane, Mechanically alloyed high entropy alloys: existing challenges and opportunities. *J. Market. Res.* **17**, 2431–2456 (2022). <https://doi.org/10.1016/j.jmrt.2022.01.141>
9. H. Song, F. Tian, Q.M. Hu, L. Vitos, Y. Wang, J. Shen, N. Chen, Local lattice distortion in high-entropy alloys. *Phys. Rev. Mater.* (2017). <https://doi.org/10.1103/PhysRevMaterials.1.023404>
10. Y. Zhang, *High-entropy materials: advances and applications* (CRC Press, Boca Raton, 2023)
11. H. Khanchandani, P. Sharma, R. Kumar, O. Maulik, V. Kumar, Effect of sintering on phase evolution in AlMgFeCuCrNi_{4.75} high entropy alloy. *Adv. Powder Technol.* (2016). <https://doi.org/10.1016/j.apt.2016.01.001>
12. M. Wu, Z. Li, B. Gault, P. Munroe, I. Baker, The effects of carbon on the phase stability and mechanical properties of heat-treated FeNiMnCrAl high entropy alloys. *Mater. Sci. Eng., A.* **748**, 59–73 (2019). <https://doi.org/10.1016/j.msea.2019.01.083>
13. J. Chen, Z. Yao, X. Wang, Y. Lu, X. Wang, Y. Liu, X. Fan, Effect of C content on microstructure and tensile properties of as-cast CoCrFeMnNi high entropy alloy. *Mater. Chem. Phys.* **210**, 136–145 (2018). <https://doi.org/10.1016/j.matchemphys.2017.08.011>
14. L. Chen, Z. Li, P. Dai, P. Fu, J. Chen, Q. Tang, Effects of carbon addition on microstructure and mechanical properties of $\text{Fe}_{50}\text{Mn}_{30}\text{Co}_{10}\text{Cr}_{10}$ high-entropy alloy prepared by powder metallurgy. *J. Market. Res.* **20**, 73–87 (2022). <https://doi.org/10.1016/j.jmrt.2022.07.067>
15. T.D. Huang, L. Jiang, C.L. Zhang, H. Jiang, Y.P. Lu, T.J. Li, Effect of carbon addition on the microstructure and mechanical properties of CoCrFeNi high entropy alloy. *Sci China Technol Sci.* **61**, 117–123 (2018). <https://doi.org/10.1007/s11431-017-9134-6>
16. J. Zhou, H. Liao, H. Chen, A. Huang, Carbon-alloyed $\text{Fe}_{35}\text{Mn}_{10}\text{Cr}_{20}\text{Ni}_{35}$ high entropy alloy synthesized by mechanical alloying plus spark plasma sintering. *J. Alloys Compd.* **859**, 157851 (2021). <https://doi.org/10.1016/j.jallcom.2020.157851>
17. W. Ji, W. Wang, H. Wang, J. Zhang, Y. Wang, F. Zhang, Z. Fu, Alloying behavior and novel properties of CoCrFeNiMn high-entropy alloy fabricated by mechanical alloying and spark plasma sintering. *Intermetallics (Barking)*. **56**, 24–27 (2015). <https://doi.org/10.1016/j.intermet.2014.08.008>

18. F. Otto, A. Dlouhý, K.G. Pradeep, M. Kuběnová, D. Raabe, G. Eggeler, E.P. George, Decomposition of the single-phase high-entropy alloy CrMnFeCoNi after prolonged anneals at intermediate temperatures. *Acta Mater.* **112**, 40–52 (2016). <https://doi.org/10.1016/j.actamat.2016.04.005>
19. R. Badji, M. Bouabdallah, B. Bacroix, C. Kahloun, B. Belkessa, H. Maza, Phase transformation and mechanical behavior in annealed 2205 duplex stainless steel welds. *Mater. Charact.* **59**, 447–453 (2008). <https://doi.org/10.1016/j.matchar.2007.03.004>
20. T.H. Chen, J.R. Yang, Effects of solution treatment and continuous cooling on β -phase precipitation in a 2205 duplex stainless steel. *Mater. Sci. Eng. A.* **311**(1–2), 28–41 (2001)
21. Y. Ikeda, I. Tanaka, ω structure in steel: a first-principles study. *J. Alloys Compd.* **684**, 624–627 (2016). <https://doi.org/10.1016/j.jallcom.2016.05.211>
22. C. Wagner, A. Ferrari, J. Schreuer, J.P. Couzinié, Y. Ikeda, F. Körmann, G. Eggeler, E.P. George, G. Laplanche, Effects of Cr/Ni ratio on physical properties of Cr-Mn-Fe-Co-Ni high-entropy alloys. *Acta Mater.* (2022). <https://doi.org/10.1016/j.actamat.2022.117693>
23. Y.H. Zhang, Y. Zhuang, A. Hu, J.J. Kai, C.T. Liu, The origin of negative stacking fault energies and nano-twin formation in face-centered cubic high entropy alloys. *Scr. Mater.* **130**, 96–99 (2017). <https://doi.org/10.1016/j.scriptamat.2016.11.014>
24. X. Li, X. Hao, C. Jin, Q. Wang, X. Deng, H. Wang, Z. Wang, The determining role of carbon addition on mechanical performance of a non-equiatom high-entropy alloy. *J. Mater. Sci. Technol.* **110**, 167–177 (2022). <https://doi.org/10.1016/j.jmst.2021.09.005>
25. B. Gwalani, V. Soni, M. Lee, S.A. Mantri, Y. Ren, R. Banerjee, Optimizing the coupled effects of Hall-Petch and precipitation strengthening in a Al_{0.3}CoCrFeNi high entropy alloy. *Mater. Des.* **121**, 254–260 (2017). <https://doi.org/10.1016/j.matdes.2017.02.072>
26. Z. Li, Interstitial equiatom high-entropy alloys: carbon content, microstructure, and compositional homogeneity effects on deformation behavior. *Acta Mater.* **164**, 400–412 (2019). <https://doi.org/10.1016/j.actamat.2018.10.050>
27. Z. Li, F. Körmann, B. Grabowski, J. Neugebauer, D. Raabe, Ab initio assisted design of quinary dual-phase high-entropy alloys with transformation-induced plasticity. *Acta Mater.* **136**, 262–270 (2017). <https://doi.org/10.1016/j.actamat.2017.07.023>
28. Z. Li, K.G. Pradeep, Y. Deng, D. Raabe, C.C. Tasan, Metastable high-entropy dual-phase alloys overcome the strength-ductility trade-off. *Nature.* **534**, 227–230 (2016). <https://doi.org/10.1038/nature17981>
29. G.N. Kirby, D.L. Sponseller, L.H. Van Vlack, The relative effects of chromium, molybdenum, and tungsten on the occurrence of ω -phase in Ni-Co-Cr alloys. *Metall. Trans.* **5**(6), 1477–1494 (1974)
30. Y. Chew, G.J. Bi, Z.G. Zhu, F.L. Ng, F. Weng, S.B. Liu, S.M.L. Nai, B.Y. Lee, Microstructure and enhanced strength of laser aided additive manufactured CoCrFeNiMn high entropy alloy. *Mater. Sci. Eng., A.* **744**, 137–144 (2019). <https://doi.org/10.1016/j.msea.2018.12.005>
31. B.C. De Cooman, Y. Estrin, S.K. Kim, Twinning-induced plasticity (TWIP) steels. *Acta Mater.* **142**, 283–362 (2018)
32. I. Gutierrez-Urrutia, D. Raabe, Dislocation and twin substructure evolution during strain hardening of an Fe-22 wt.% Mn-0.6 wt.% C TWIP steel observed by electron channeling contrast imaging. *Acta Mater.* **59**, 6449–6462 (2011). <https://doi.org/10.1016/j.actamat.2011.07.009>
33. S. Mahajan, M.L. Green, D. Brasen, A model for the FCC→HCP transformation, its applications, and experimental evidence. *Metall. Trans. A.* **8**(2), 283–293 (1977)
34. A. Kisko, R.D.K. Misra, J. Talonen, L.P. Karjalainen, The influence of grain size on the strain-induced martensite formation in tensile straining of an austenitic 15Cr-9Mn-Ni-Cu stainless steel. *Mater. Sci. Eng., A.* **578**, 408–416 (2013). <https://doi.org/10.1016/j.msea.2013.04.107>
35. J. Moon, J.M. Park, J.W. Bae, H.S. Do, B.J. Lee, H.S. Kim, A new strategy for designing immiscible medium-entropy alloys with excellent tensile properties. *Acta Mater.* **193**, 71–82 (2020). <https://doi.org/10.1016/j.actamat.2020.03.050>
36. T. Yang, Z. Tang, X. Xie, R. Carroll, G. Wang, Y. Wang, K.A. Dahmen, P.K. Liaw, Y. Zhang, Deformation mechanisms of Al_{0.1}CoCrFeNi at elevated temperatures. *Mater. Sci. Eng., A.* **684**, 552–558 (2017). <https://doi.org/10.1016/j.msea.2016.12.110>
37. O.D. Sherby, P.M. Burke, Mechanical behavior of crystalline solids at elevated temperature. *Progr. Mater. Sci.* **13**, 323–390 (1968)
38. M.H. Chuang, M.H. Tsai, W.R. Wang, S.J. Lin, J.W. Yeh, Microstructure and wear behavior of Al_xCo_{1.5}CrFeNi_{1.5}Ti_y high-entropy alloys. *Acta Mater.* **59**, 6308–6317 (2011). <https://doi.org/10.1016/j.actamat.2011.06.041>
39. W. Chen, N. Li, F. Wang, J. Gu, J. He, M. Song, On the dual-stage partial recrystallization and the corresponding mechanical response of the Cantor alloy. *J. Alloys Compd.* (2022). <https://doi.org/10.1016/j.jallcom.2022.165651>
40. K. Ming, X. Bi, J. Wang, Microstructures and deformation mechanisms of Cr₂₆Mn₂₀Fe₂₀Co₂₀Ni₁₄ alloys. *Mater. Charact.* **134**, 194–201 (2017). <https://doi.org/10.1016/j.matchar.2017.10.022>
41. A. Monshi, M.R. Foroughi, M.R. Monshi, Modified scherrer equation to estimate more accurately nano-crystallite size using XRD. *World J. Nano Sci. Eng.* (2012). <https://doi.org/10.4236/wjnse.2012.23020>
42. V.S. Vinila, J. Isac, Synthesis and structural studies of superconducting perovskite GdBa₂Ca₃Cu₄O_{10.5+d} nanosystems, in Design, Fabrication, and Characterization of Multifunctional Nanomaterials (2021)
43. G. Laplanche, S. Berglund, C. Reinhart, A. Kostka, F. Fox, E.P. George, Phase stability and kinetics of σ -phase precipitation in CrMnFeCoNi high-entropy alloys. *Acta Mater.* **161**, 338–351 (2018). <https://doi.org/10.1016/j.actamat.2018.09.040>
44. X. Qin, C.H. Shek, heterogeneous structure design to strengthen carbon-containing CoCrFeNi high entropy alloy. *Acta Metallurgica Sinica (English Letters)*. **34**, 1503–1510 (2021). <https://doi.org/10.1007/s40195-021-01268-4>
45. D. Choudhuri, S. Shukla, W.B. Green, B. Gwalani, V. Ageh, R. Banerjee, R.S. Mishra, Crystallographically degenerate B2 precipitation in a plastically deformed fcc-based complex concentrated alloy. *Mater. Res. Lett.* **6**, 171–177 (2018). <https://doi.org/10.1080/21663831.2018.1426649>
46. D.L. Medlin, S.M. Foiles, D. Cohen, A dislocation-based description of grain boundary dissociation: application to a 90° 110 tilt boundary in gold. *Acta Materialia.* **49**(18), 3689–3697 (2001)
47. S. Wei, J. Kim, C.C. Tasan, Boundary micro-cracking in metastable Fe₄₅Mn₃₅Co₁₀Cr₁₀ high-entropy alloys. *Acta Mater.* **168**, 76–86 (2019). <https://doi.org/10.1016/j.actamat.2019.01.036>
48. L. Guo, X. Ou, S. Ni, Y. Liu, M. Song, Effects of carbon on the microstructures and mechanical properties of FeCoCrNiMn high entropy alloys. *Mater. Sci. Eng., A.* **746**, 356–362 (2019). <https://doi.org/10.1016/j.msea.2019.01.050>
49. Z. Li, C.C. Tasan, H. Springer, B. Gault, D. Raabe, Interstitial atoms enable joint twinning and transformation induced plasticity in strong and ductile high-entropy alloys. *Sci. Rep.* (2017). <https://doi.org/10.1038/srep40704>
50. S.J. Sun, Y.Z. Tian, H.R. Lin, H.J. Yang, X.G. Dong, Y.H. Wang, Z.F. Zhang, Transition of twinning behavior in CoCrFeMnNi high entropy alloy with grain refinement. *Mater. Sci. Eng., A.* **712**, 603–607 (2018). <https://doi.org/10.1016/j.msea.2017.12.022>
51. J.Y. He, H. Wang, H.L. Huang, X.D. Xu, M.W. Chen, Y. Wu, X.J. Liu, T.G. Nieh, K. An, Z.P. Lu, A precipitation-hardened

- high-entropy alloy with outstanding tensile properties. *Acta Mater.* **102**, 187–196 (2016). <https://doi.org/10.1016/j.actamat.2015.08.076>
52. W. Lu, C.H. Liebscher, G. Dehm, D. Raabe, Z. Li, Bidirectional transformation enables hierarchical nanolaminate dual-phase high-entropy alloys. *Adv. Mater.* (2018). <https://doi.org/10.1002/adma.201804727>
53. R.S. Ganji, P. Sai Karthik, K. Bhanu Sankara Rao, K.V. Rajulapati, Strengthening mechanisms in equiatomic ultrafine grained AlCoCrCuFeNi high-entropy alloy studied by micro- and nanoindentation methods. *Acta Mater.* **125**, 58–68 (2017). <https://doi.org/10.1016/j.actamat.2016.11.046>
54. M.H. Tsai, J.W. Yeh, High-entropy alloys: a critical review. *Mater. Res. Lett.* **2**, 107–123 (2014). <https://doi.org/10.1080/21663831.2014.912690>

Publisher's Note Springer Nature remains neutral with regard to jurisdictional claims in published maps and institutional affiliations.

Springer Nature or its licensor (e.g. a society or other partner) holds exclusive rights to this article under a publishing agreement with the author(s) or other rightsholder(s); author self-archiving of the accepted manuscript version of this article is solely governed by the terms of such publishing agreement and applicable law.